Supporting information for Water Ligands Regulate the Redox Leveling Mechanism of the Oxygen-Evolving Complex of Photosystem II

Jinchan Liu,[†] Ke R. Yang,[‡] Zhuoran Long,[¶] William H. Armstrong,[§] Gary W. Brudvig,[†,¶] and Victor S. Batista[*,¶]

[†]*Department of Molecular Biophysics and Biochemistry, Yale University, New Haven, CT, 06520, USA*

[‡]*Key Laboratory of Advanced Energy Materials Chemistry (Ministry of Education), College of Chemistry, Nankai University, Tianjin, 300071, China*

[¶]*Department of Chemistry, Yale University, New Haven, CT, 06520, USA*

[§]*Department of Chemistry, Boston College, Chestnut Hill, MA, 02467, USA*

E-mail: victor.batista@yale.edu

Method

Quantum Mechanics/Molecular Mechanics

We built our Quantum Mechanics/Molecular Mechanics (QM/MM) model from coordinates provided by Umena et al.[1] (PDBID: 3WU2) as described previously.[2] This model of ∼2500 atoms includes residues whose alpha carbons are within 15 Å of the OEC, using ACE and NMA as capping residues with fixed positions during the calculations. We include the OEC, one Cl^- ion, 14 waters, the side chain of D1-D61, D1-Y161, D1-N181, D1-E189, D1-H190, D1-H332, D1-E333, D1-H337, D1-D342, D1-A344, CP43-E354, CP43-R357, D2-K317 and the whole residue of D1-S169, D1-D170, D1-G171 in the QM layer. For the calculations involving electron transfer from Mn1 or Mn4 to $Y_Z^\bullet$, D1-Q165 and D1-N298 are included in the QM layer to establish a proper electrostatic environment for the $Y_Z^\bullet$.[3] The structures are optimized using the ONIOM method[4] in Gaussian16:[5] The QM layer employs DFT level of theory using the B3LYP exchange-correlation functional[6–9] and the LanL2DZ pseudopotential and basis set for Mn and Ca atoms,[10,11] the 6-31G(d) basis set for O and Cl,[12] the 6-31G for H, C and N.[13–15] The MM layer is calculated using the AMBER force field.[16] Structure visualization was performed using VMD.[17]

All QM/MM optimized structures are available in the QMMM folder of our github page built for this paper: https://github.com/JinchanLiu/S2toS3/.

Molecular Dynamics

System Preparation and Parameterization

We construct our MD system with psfgen from the 1.9 Å resolution X-ray crystal structure of *Thermostichus vulcanus* PSII (PDBID: 3WU2),[1] assisted by information from other X-Ray structures (PDBID: 4V62 and 4UB6).[18,19] Chain A to Z of PDB 3WU2 is used to build our PSII monomer system. The X-ray structure is first oriented to have the protein hydrophobic surface on x-y plane to match the lipid bilayer building around the PSII

monomer. To minimize box dimension of our system and save computational resources, the PSII is further rotated in the x-y plane to make the longest dimension of the protein in the x-y plane fall on the diagonal of the x-y plane. The final system has a box dimension of 143Å×144Å×140Å with 302k atoms.

Protein. Missing residues in PDB 3WU2 are constructed by referencing other X-ray structures, such as PDB 4UB6 and 4V62. In instances where no coordinate information was available, we utilize psfgen to generate coordinates for missing regions less than 4 amino acids in length. Notably, any missing regions larger than 4 amino acids are exclusively located at the N-termini and are excluded from the system, with the N-termini capped with ACE patch. For the protonation states of ASP, GLU, ARG and LYS, we considered protonation states from MCCE calculations by Kaur et al.[20] and predicted by propKa.[21] After careful visualization, A-E65, B-D380 and O-E97 are protonated. All CYS are neutral with a disulfide bond added between O-C19 and O-C44. For HIS, we used the protonation states from Kaur et al.:[20] A-H92, A-H304, A-H337, B-H343, C-H74, C-H398, O-H228 and U-H81 are modelled as HSP; A-H195, A-H252, B-H157, B-H201, D-H61 , D-H87 , D-H189, D-H336, O-H231 and V-H118 are modelled as HSE; all other HIS are modelled as HSD. CHARMM36m force field is used for protein.[22]

Pigments. Chlorophyll-a, pheophytin-a, plastoquinone-9 are modelled with the topology and parameter files from Guerra et al..[23] All 11 β-carotenes from PDB 3WU2 are included and 2 extra are added according to PDB 4V62. The 2 extra β-carotenes are modelled as unknown ligands in PDB 3WU2. CgenFF is used for parameterizing β-Carotene.[24]

Heme and non-heme iron are modelled with the topology and parameter files from Adam et al..[25]

Lipids. We include all MGDG, DGDG, SQDG and PG from PDB 3WU2 in our MD system with missing lipid tails or head groups patched. New topology files for these lipids are written because of the inconsistency in atom names between CHARMM force field and X-ray structures. Six extra lipids are added according to PDB 4V62 (residue 401 1811 5042

3585 2562 5525 when visualized in VMD). Two extra lipids are manully added to maintain the stability of the hydrophobic pocket formed between D1 (chain A), b599b (chain F), psbJ (chain J) and prevent water coming in. The lipids in the membrane bilayer are built by CHARMM-GUI.[26,27] We use a lipid composition of MGDG:DGDG:SQDG:PG=8:4:1:2 for the outer leaflet and MGDG:DGDG:SQDG:PG=8:4:8:1 for the inner leaflet.[28,29] For each type of lipid, we assign lipid tails with certain degrees of unsaturation and numbers of carbons according to Sakurai et al.[30] (Table S1). CHARMM36 force field is used for all lipids.[31]

Table S1: Amount of lipids of different lipid tails in the outer leaflet and the inner leaflet built by CHARMM-GUI.

	Outer Leaflet				**Inner Leaflet**			
	MGDG	DGDG	SQDG	PG	MGDG	DGDG	SQDG	PG
16:0/16:0	31	15	9	8	22	10	42	3
16:0/18:1	59	32	3	13	46	18	21	5
16:1/16:1	21	11			14	6		
18:0/18:1	11	3	3	6	7	4	14	2
16:0/16:1				4				2

The OEC and its ligands. The coordinates for the OEC as well as its surrounding amino acids and waters are taken from QM/MM calculations. Bond and angle terms of the OEC as well as between the OEC and the ligands are added to maintain the geometry (Table S2, S3). The centers for bonds and angles adopts the number from QM calculations. The constants for bonds and angles are adapted from the parameters for a manganese-vanadium water oxidation catalyst by Cárdenas et al..[32] The point charges for the OEC and its coordinating ligands adopt the ESP charges from our QM/MM calculations. The Lennard-Jones parameters for the Mn ions are adapted from Won.[33]

Water and ions. All water molecules solved by PDB 3WU2 are included and all oxygens of glycerol molecules are modelled as water (segname WXG in our files). A water box of 62k waters is used to solvate the system. 355 Na^+ and 181 Cl^- are added to the system to neutralize and maintain a salt concentration of 0.15M. TIP3P model is used for water[34] and CHARMM36 force field is used for ions with updated NBFIX terms.[35]

Table S2: The bond constants for the OEC and its ligands.

Bond Type		Constant
Mn^{III}	µ-oxo	350 kcal/mol/Å^2
Mn^{III}	OC/NR2	250 kcal/mol/Å^2
Mn^{IV}	µ-oxo	400 kcal/mol/Å^2
Mn^{IV}	OC/NR2	300 kcal/mol/Å^2
Ca	µ-oxo	250 kcal/mol/Å^2
Ca	OC/NR2	150 kcal/mol/Å^2

Table S3: The angle constants for the OEC and its ligands.

Angle Type			Constant
Mn/Ca	µ-oxo	Mn/Ca	600 kcal/mol/rad^2
µ-oxo	Mn/Ca	µ-oxo	600 kcal/mol/rad^2
µ-oxo	Mn/Ca	OC/NR2	200 kcal/mol/rad^2
OC/NR2	Mn/Ca	OC/NR2	150 kcal/mol/rad^2
Mn/Ca	OC	CC	200 kcal/mol/rad^2

All files required to reproduce our results can be found in the MD folder of our github page. All topology and parameter files for the OEC can be found in the MD/toppar/ folder. An example script of mutating the PSII as needed and assembling the whole system is provided in the MD/modifyMDsys/ folder.

MD protocal

Equilibration and Solvation

The system is equilibrated with the different components of the system gradually relaxed.

Step 1: The system at S_1 is minimized for 5000 steps with everything constrained except for the following: hydrogens of water molecules whose coordinates are not taken from QM/MM, cofactors from PDB 4V62 and 4UB6, the two extra lipids manually added to the hydrophobic pocket formed by b599b (chain F) and psbJ (chain J), the protein residues guessed by psfgen.

Step 2: The system at S_1 is minimized for 5000 steps, heated up to 300K, and equilibrated

for 1 ns in the NVT ensemble with the lipid tails added to the relaxed component.

Step 3: The system at S_1 is minimized for 5000 steps and equilibrated for 10ns at 300K in the NPT ensemble with the following remain restrained: non-hydrogen atoms of protein, cofactors and water determined by PDB 3WU2 and the OEC as well as its surrounding amino acids and waters whose coordinates are taken from QM/MM.

Step 4: The system at S_1 is minimized for 1000 steps and heated up to 350K in the NPT ensemble to sample water conformation. An extra water is added in this step (segname WA) in the case where one water was sampling two sites. The following remain restrained during this step: non-hydrogen atoms of protein determined by PDB 3WU2 and the OEC as well as its surrounding amino acids and waters taken from QM/MM. The system is then cooled down to 300K: it is equilibrated for 0.5 ns for every 10K. And then the system is further equilibrated for 5 ns at 300K.

Step 5-1: The system at S_1 is minimized for 1000 steps and equilibrated for 10ns at 300K with the protein backbone restrained, together with the atoms whose coordinates are taken from QM/MM. The resulting coordinate for this step is provided in the MD folder of the github page for this paper, named 3wu2_PSII_S1_addwat1.pdb

Step 5-2: Using the coordinate of 3wu2_PSII_S1_addwat1.pdb, we build the system at $S_2^n cY_Z^\bullet$ (S2DW), with W10 binding to the Mn4 and WS10 is left vacancy. The system at S2DW is minimized for 1000 steps and equilibrated for 10ns at 300K with the protein backbone restrained, together with the atoms whose coordinates are taken from QM/MM. The starting coordinate for this step is provided, named 3wu2_PSII_S2DW.pdb

Step 6: The system is minimized for 1000 steps and equilibrated with only atoms whose coordinates are taken from QM/MM constrained. The resulting coordinate from this step is provided, named 3wu2_PSII_S2DW_EQed.pdb

A distance restraint between OD1-D61 and Mn4 is added with a force constant of 50 $\text{kcal}/(\text{mol} \cdot \text{Å}^2)$ to represent the strong hydrogen bond between W1 and D61 as well as the ligand binding between W1 and Mn4.[2] Without this restraints, D61 will fall apart from Mn4,

with two waters in between Mn4 and D61 and the Cl1 will move away.[36]

Another distance restraint between NE2-H190 and OH-Y161 is added with a force constant of 50 kcal/(mol $\cdot$ Å^2) as emphasized by Ishikita and Saito.[37]

The replenishment of W10

After the six steps of equilibration, we performed 50 replicas of 500 ps simulations to sample the replenishment of W10 with the two distance restraints. An example of the NAMD configuration file is provided, named 3wu2_PSII_S2DW_SW_rep1.conf. The replenishment is characterized by water occupancy. The occupancy of a specific water molecule at a given water site at time t is calculated as the number of replicas in which this particular water molecule is present at the designated site at time t, divided by the total number of replicas. A water is count as "present at the designated site" if it is within 1.7 Å of the water site. Therefore, a water may be present at two water sites at the same time, so that the water occupancy at a water site at time t may add up to more than 100%.

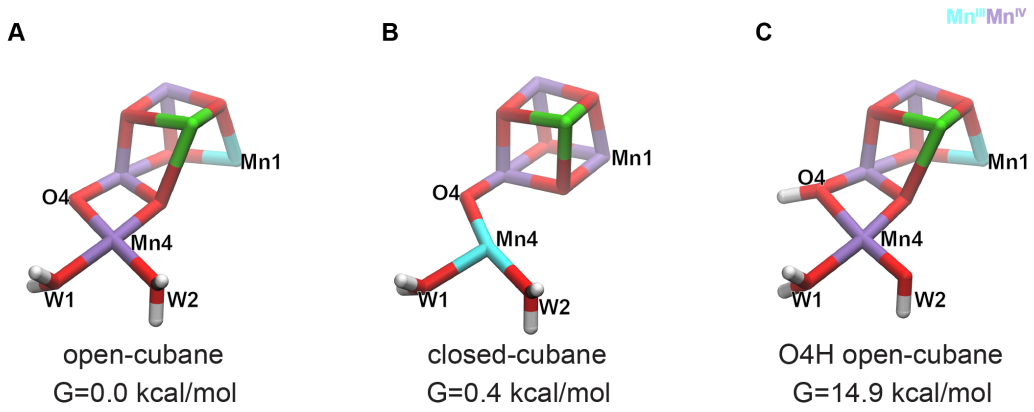

Figure S1: Possible $S_2^+Y_Z$ states giving rise to the EPR signals. **(A)** The low-spin open-cubane isomer proposed to give rise to the g=2.0 multiline EPR signal **(B)** The high-spin closed-cubane isomer and **(C)** The O4H open-cubane isomer potentially giving rise to the g=4.1 signal. The closed-cubane is 1.4 kcal/mol higher than the open-cubane while the O4H open-cubane is 14.9 kcal/mol higher, which makes it difficult to present.

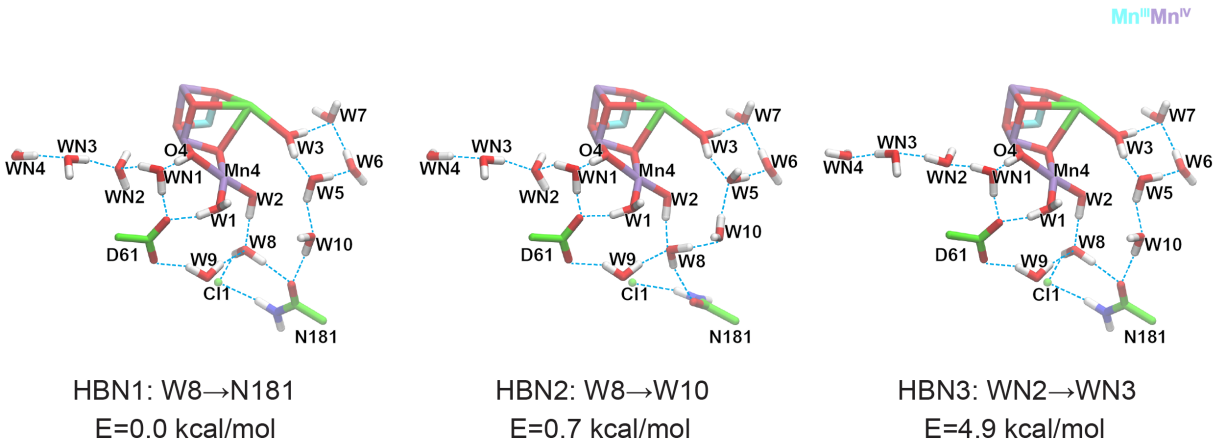

Figure S2: Three hydrogen bond networks (HBNs) at the O4H open-cubane $S_2^+Y_Z$ state. HBN1 has W8 donating hydrogen bonds to N181 and Cl1, WN3 accepting a hydrogen bone from WN4 and donating a hydrogen bond to WN2, and is the most energetically favorable one. HBN2 has W8 donating hydrogen bonds to N181 and W10. HBN3 has WN3 donating a hydrogen bond to WN4 and accepting a hydrogen bond from WN2, resulting in one O-H bond of WN4 point to a hydrophobic pocket. This reorientation of WN4 leads to overall one less hydrogen bond compared to HBN1, and therefore, is unfavorable as discussed previously.[38]

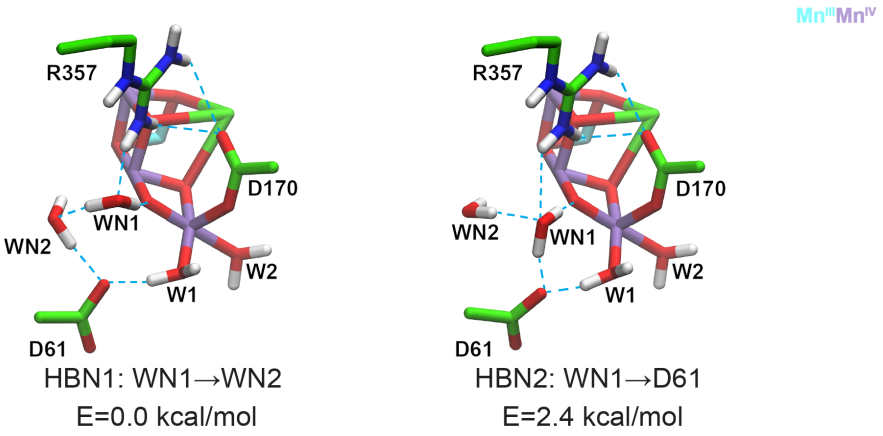

Figure S3: Two hydrogen bond networks at the open-cubane $S_2^+Y_Z$ state. The left one has WN1 donating hydrogen bonds to O4 of the OEC and WN2, while the right one has WN1 donating hydrogen bonds to O4 and D61. Although the right one is the HBN adopted for the S_1 state, the HBN on the left is 2.4 kcal/mol more favorable at $S_2^+oY_Z$ state and is adopted in all of our S_2 state structures, except when O4 is protonated.

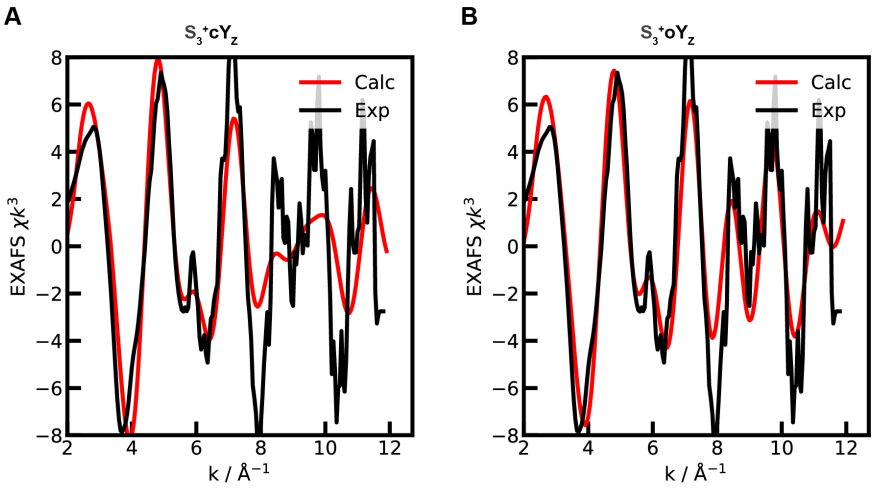

Figure S4: Simulated EXAFS of the **(A)** $S_3^+cY_Z$ state and **(B)** $S_3^+oY_Z$ state we obtained from QM/MM optmization.

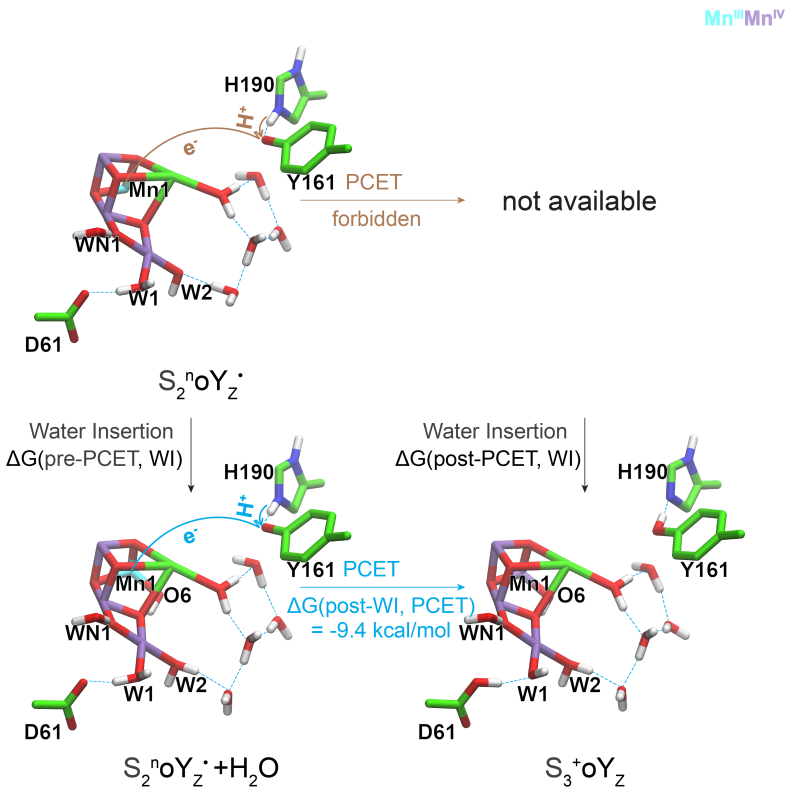

Figure S5: The proton-coupled electron transfer (PCET) at $S_2^nY_Z^\bullet$ for the open-cubane state, with the electron transfer from $Mn1^{III}$ to $Y_Z^\bullet$ coupled by a proton transfer from H190 to $Y_Z^\bullet$. Without the water insertion, $S_3^+oY_Z$-H_2O is not sufficiently stable to manifest, suggesting the PCET is forbidden for the open-cubane without the presence of water. This is likely due to the charge environment of Mn1 disfavor a $Mn1^{IV}$. In comparison, The free energy change for the PCET at the open-cubane with the presence of water is -9.4 kcal/mol. Overall, these open-cubane structures suggest that the incoorporation of the water promotes the PCET, consistent with the analysis on the closed-cubane structures.

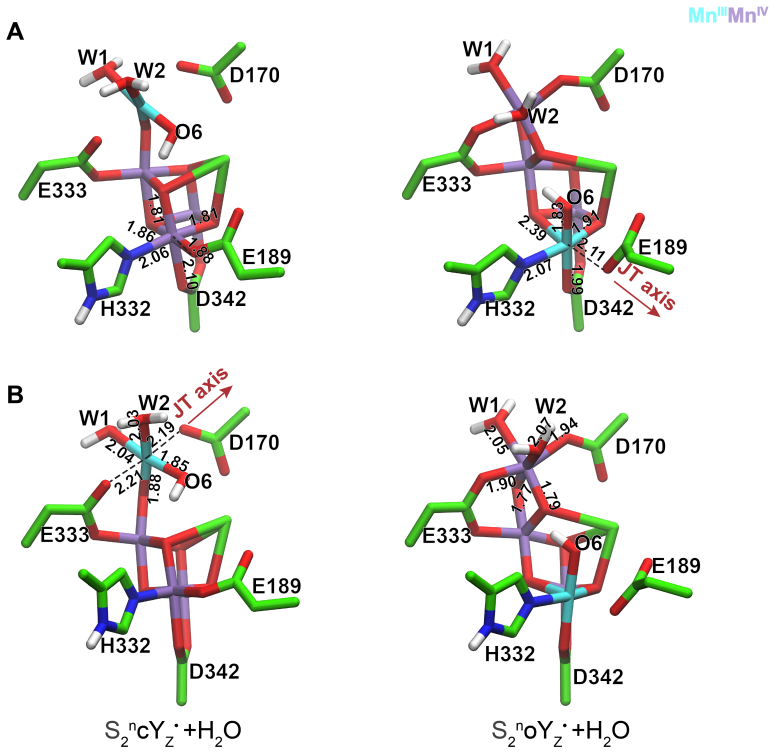

Figure S6: The distances between Mn ions and their ligands for $S_2^n cY_Z^{\bullet}+H_2O$ and $S_2^n oY_Z^{\bullet}+H_2O$. **(A)** The $Mn1^{IV}$ in $S_2^n cY_Z^{\bullet}+H_2O$ and the $Mn1^{III}$ in $S_2^n oY_Z^{\bullet}+H_2O$. The $Mn1^{III}$ adopts a Jahn-Teller axis along the O3-Mn1-E189 axis, breaking a μ-oxo bridge and accounting for the destabilization of $S_2^n oY_Z^{\bullet}+H_2O$. **(B)** The $Mn4^{III}$ in $S_2^n cY_Z^{\bullet}+H_2O$ and the $Mn4^{IV}$ in $S_2^n oY_Z^{\bullet}+H_2O$. The $Mn4^{III}$ adopts a Jahn-Teller axis along the D170-Mn4-E333 axis.

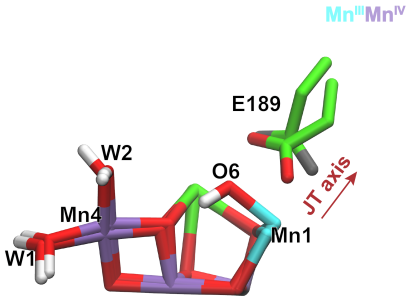

Figure S7: Superposition of $S_2^n oY_Z^{\bullet}$ and $S_2^n oY_Z^{\bullet}+H_2O$ showing the unbinding of E189 in $S_2^n oY_Z^{\bullet}+H_2O$.

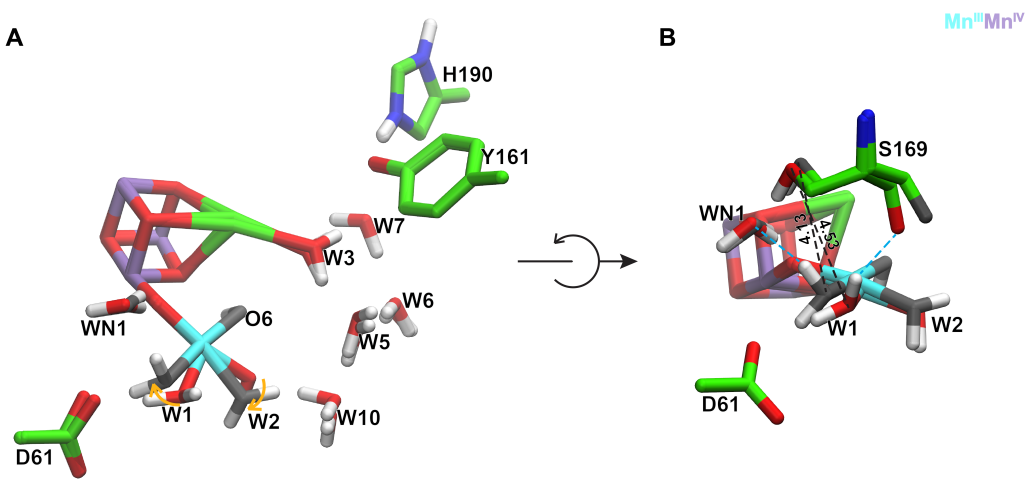

Figure S8: The difference in hydrogen bond network between $S_2^n cY_Z^\bullet$ and $S_2^n cY_Z^\bullet + H_2O$. The oxygen of major change in $S_2^n cY_Z^\bullet + H_2O$ is labelled in grey. **(A)** The rotation of W1 and W2 in $S_2^n cY_Z^\bullet + H_2O$ to accommodate O6. **(B)** The rotation of W1 and W2 breaks the hydrogen bond between W1 and the backbone of S169, resulting in a new hydrogen bond between W1 and WN1. This change brings W1 closer to OH-S169, from 4.53 Å to 4.12 Å. A change in this distance is described by Hussein et al.[39] during the $S_2 \rightarrow S_3$ transition.

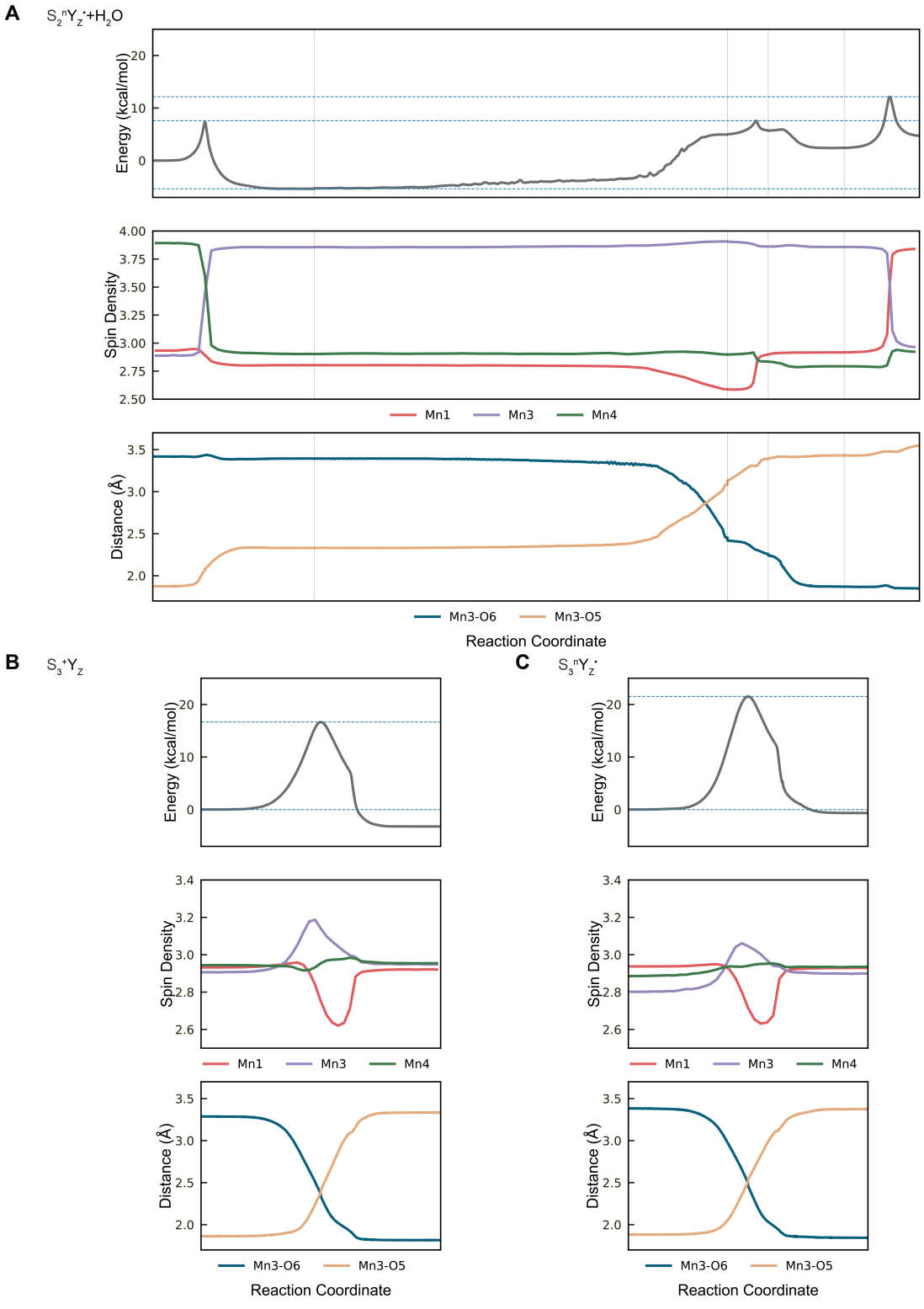

Figure S9: The changes of Mn spin densities and Mn3-O6 and Mn3-O5 distances during the closed-cubane to open-cubane isomerization at **(A)** $S_2^nY_Z^{\bullet}+H_2O$, **(B)** $S_3^+Y_Z$ and **(C)** $S_3^nY_Z^{\bullet}$.

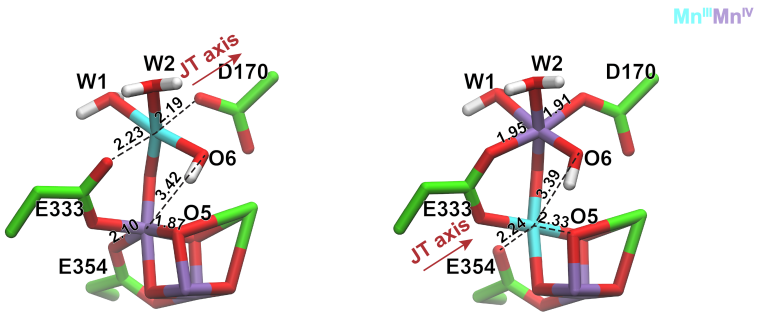

Figure S10: For the isomerization at $S_2^n Y_Z^{\bullet}$+H_2O from the closed-cubane to the open-cubane, we identified an electron transfer from $Mn4^{III}$ to $Mn3^{IV}$, leading to the Jahn-Teller axis shift from the D170-Mn4-E333 axis to the O5/O6-Mn3-E354 axis.

Table S4: The numbering of water molecules.

Batista	chain & resid in PDB 3WU2	Yuno	resid in our MD	resid in our QM/MM
W1	A595	W1	95	190
W2	A624	W2	-	189
W3	A601	W3	69	187
W4	A544	W4	44	186
W5	A509	W24	9	188
W6	A567	W23	67	198
W7	A564	W25	64	197
W8	A609	W22	109	192
W9	A621	W21	121	193
W10	A568	W61	68	199
W11	A572	W62	72	191
WN1	A511	W19	11	194
WN2	C633	W20	512	195
WN3	A605	W48	105	196
WN4	A516	W49	16	200
WL1	A623	W28	499	175
WL2	A597	W26	97	185
WL3	A508	W27	8	176
WL4	A562	W29	62	178
WL5	A576	W30	76	177

Table S5: The relative energy for the states before and after the PCET, pre- and post-water insertion at varying spin states.

QM size	System	Energy (kcal/mol)							
213 atoms	$S_2^n cY_Z^\bullet$	ααααα	0.00	αααααβ	0.01	αααβα	-1.00	αβαβα	0.46
	$S_2^n oY_Z^\bullet$	ααααα	-4.59	αααααβ	-4.58	αααββ	-5.29	αβαββ	-5.54
	$S_3^+ cY_Z$-H_2O			αααα	13.10	αααβ	10.87	αβαβ	12.93
	$S_3^+ oY_Z$-H_2O	not available							
216 atoms	$S_2^n cY_Z^\bullet$+H_2O	ααααα	0.00	αααααβ	0.00	αααβα	-0.93	αβαβα	0.45
	$S_2^n oY_Z^\bullet$+H_2O	ααααα	8.07	αααααβ	8.07	αααββ	7.20	αβαββ	8.46
	$S_3^+ cY_Z$			αααα	3.27	αααβ	3.00	αβαβ	5.04
	$S_3^+ oY_Z$			αααα	-4.12	αααβ	-5.20	αβαβ	-4.36

Table S6: The relative free energy for the states before and after the PCET, pre- and post-water insertion at varying spin states.

QM size	System	Free Energy (kcal/mol)							
213 atoms	$S_2^n cY_Z^\bullet$	ααααα	0.00	αααααβ	0.10	αααβα	-0.50	αβαβα	1.87
	$S_2^n oY_Z^\bullet$	ααααα	-3.02	αααααβ	-3.01	αααββ	-3.33	αβαββ	-2.62
	$S_3^+ cY_Z$-H_2O			αααα	12.58	αααβ	10.93	αβαβ	13.85
	$S_3^+ oY_Z$-H_2O	not available							
216 atoms	$S_2^n cY_Z^\bullet$+H_2O	ααααα	0.00	αααααβ	0.11	αααβα	-0.39	αβαβα	1.86
	$S_2^n oY_Z^\bullet$+H_2O	ααααα	11.34	αααααβ	11.28	αααββ	10.82	αβαββ	12.91
	$S_3^+ cY_Z$			αααα	6.03	αααβ	6.19	αβαβ	9.08
	$S_3^+ oY_Z$			αααα	1.92	αααβ	1.23	αβαβ	3.06

Table S7: The relative energy of the states along the closed to open-cubane transition at $S_2^n Y_Z^{\bullet}$+H_2O at varying spin states.

QM size	System	Energy (kcal/mol)			
		ααααα	αααβα	αβααα	αβαβα
200	4443-closed-cubane (A1)	0.00	-0.99	1.32	
	4434-closed-cubane (A3)	-5.35	-5.98	-5.81	-6.45
	4434-open-cubane (A7)	5.65	5.87	5.09	5.06
	3444-open-cubane (A11)	5.56		6.91	5.96

Table S8: The relative free energy of the states along the closed to open-cubane transition at $S_2^n Y_Z^{\bullet}$+H_2O at varying spin states.

QM size	System	Free Energy (kcal/mol)			
		ααααα	αααβα	αβααα	αβαβα
200	4443-closed-cubane (A1)	0.00	-0.41	1.38	
	4434-closed-cubane (A3)	-4.34	-4.57	-4.69	-4.57
	4434-open-cubane (A7)	7.12	7.79	6.97	7.65
	3444-open-cubane (A11)	9.23		10.61	10.37

Magnetic structure and proton hyperfine coupling constants for A3

The magnetic structure and proton hyperfine coupling constants were calculated for state A3 (4434-closed-cubane) using the broken symmetry approach following our previous work[2] and the original work by Pantazis et al.[40] with the ORCA 5.0.4 package.[41–43] Coordinates of atoms in the QM region of A3 were extracted from the corresponding QM/MM model and the dangling bonds were capped with hydrogen atoms with $d_{\text{C-H}}$ = 1.00 Å and $d_{\text{N-H}}$ = 1.00 Å. The calculations were performed with the B3LYP functional[6–9] and the zeroth-order regular approximation (ZORA)[44,45] for scalar relativistic effects. The basis sets were decontracted ZORA-adapted segmented all-electron relativistically contracted (SARC) basis sets ZORA-def2-TZVP for N, O and Mn atoms and ZORA-def2-TZVP(-f) for H, C, Ca and Cl atoms. RIJCOSX approximation was applied with the SARC/J auxiliary basis sets for Coulomb fitting. The DEFGRID2 integration grid was used with special grids on H atoms for increased integral accuracy (SpecialGridIntAcc 9). The "very tight" SCF convergence criteria was used for calculating energy of Broken-symmetry spin configurations, and the "tight" SCF convergence cirteria was used for calculating EPR hyperfine coupling constants. The COSMO implicit solvent model was applied with a dielectric constant ε = 8.0 representing the protein environment around OEC.[46,47]

The four Mn centers in A3 are Mn1^{IV}, Mn2^{IV}, Mn3^{III} and Mn4^{IV}. Together with the $\text{Y}_{\text{Z}}^{\bullet}$, the 2^{n-1}=16 possible high spin and broken symmetry spin configurations are listed in Table S9. The relative energy of different spin configurations indicate that the $\text{Y}_{\text{Z}}^{\bullet}$ spin is very weakly coupled to Mn spins, and the lowest energy configuration for Mn centers is αα|βα.

The magnetic interaction between Mn centers can also be described with an effective Hamiltonian, i.e. the Heisenberg-Dirac-van Vleck (HDvV) Hailtonian:

$$H_{\text{HDvV}} = -2\sum_{i<j} J_{ij}\vec{S}_i \cdot \vec{S}_j \tag{1}$$

Table S9: Possible spin configurations, M_S, and relative energy to the high spin configuration (kcal/mol).

Spin	M_S	Energy (kcal/mol)	Spin	M_S	Energy (kcal/mol)
ααααα	7	0	ααααβ	6	0.00
αααβα	4	-0.52	αααββ	3	-0.52
ααβαα	3	-1.65	αα$\beta\alpha\beta$	2	-1.65
αβααα	4	-0.39	αβααβ	3	-0.39
βαααα	4	0.47	βαααβ	3	0.47
αβαβα	1	-0.95	αβαββ	0	-0.95
βααβα	1	-0.15	βααββ	0	-0.15
ββαααα	1	-0.99	ββααβ	0	-0.99

The exchange coupling constants (J) can be extracted with the single-value decomposition (SVD) implemented in an in-house Python script. The result in Table S10 suggests ferromagnetic coupling between Mn1-Mn2 (J_{12}), Mn1-Mn4 (J_{14}) and Mn2-Mn4 (J_{24}), and an antiferromagnetic coupling between Mn1-Mn3 (J_{13}), Mn2-Mn3 (J_{23}) and Mn3-Mn4 (J_{34}). This is consistent with the observation that αα$\beta\alpha$ is the lowest energy configuration. And again $Y_Z^\bullet$ is very weakly coupled to Mn spins as suggester by *ca.* zero values of J_{15}, J_{25}, J_{35} and J_{45}.

Table S10: Exchange coupling constants (J) among Mn centers.

	J (cm^{-1})	
J_{12}	20.8	Mn1-Mn2
J_{13}	-3.3	Mn1-Mn3
J_{14}	2.0	Mn1-Mn4
J_{15}	0.0	Mn1-$Y_Z^\bullet$
J_{23}	-27.5	Mn2-Mn3
J_{24}	0.8	Mn2-Mn4
J_{25}	0.0	Mn2-$Y_Z^\bullet$
J_{34}	-17.2	Mn3-Mn4
J_{35}	0.0	Mn3-$Y_Z^\bullet$
J_{45}	-0.0	Mn4-$Y_Z^\bullet$

These exchange coupling constants are utilized to reconstruct the HDvV Hamiltonian matrix, which is then diagonalized to obtain the site spin expectation value $\langle S_{Z,i} \rangle$. This calculation can be done with the *orca_eca* utility from the ORCA package. The isotropic hyperfine coupling constants (A_{iso}) can be calculated by scaling the "raw" results ($A_{\text{iso,BS}}$)

from broken symmetry DFT calculations with the following equation:

$$A_{\text{iso}} = \pm A_{\text{iso,BS}} \frac{\langle S_Z \rangle_{\text{BS}}}{S_i} \frac{\langle S_{Z,i} \rangle}{S_t} \tag{2}$$

where $\langle S_Z \rangle_{\text{BS}} = M_S$ which is the total M_S of the broken symmetry wavefunction.

Table S11: Spin projection factors.

		S_t	$\langle S_Z \rangle_{\text{BS}}$	S_i	$\langle S_{Z,i} \rangle$	Scaling Factor
ααβαα	$Mn1^{IV}$	3	3	1.5	1.417	0.945
	$Mn2^{IV}$			1.5	1.197	0.798
	$Mn3^{III}$			2.0	-1.376	0.688
	$Mn4^{IV}$			1.5	1.262	0.841
	$Y_Z^{\bullet}$			0.5	0.500	1.000
ααβαβ	$Mn1^{IV}$	3	2	1.5	1.417	0.630
	$Mn2^{IV}$			1.5	1.197	0.532
	$Mn3^{III}$			2.0	-1.376	0.459
	$Mn4^{IV}$			1.5	1.262	0.561
	$Y_Z^{\bullet}$			0.5	0.500	0.667

The "raw" hyperfine coupling constants are calculated with the lowest energy configurations ααβαα ($M_S = 3$) and ααβαβ ($M_S = 2$). The spin ground state has $S = 3$, and the first excited state ($S = 2$) also degenerated with the ground state (0.007 cm^{-1} in our calculation). The corresponding spin projection factors and the final scaling factors, calculated using $S_t = 3$, are provided in Table S11. The protons chosen for isotropic hyperfine coupling constant calculations are labeled in Figure S11. The raw and scaled proton hyperfine coupling constants are listed in Table S12 and S13, respectively. The direct average are also included as the two configurations are isoenergetic.

Table S12: Unscaled isotropic hyperfine coupling constants (A_{iso}) in MHz of protons in OEC ligands.

H name	$A_{\text{iso,BS,ααβαα}}$ (MHz)	$A_{\text{iso,BS,ααβαβ}}$ (MHz)
H_A	0.884	1.326
H_B	1.035	1.552
H_C	0.914	1.370
H_D	1.032	1.548
H_E	5.504	8.256

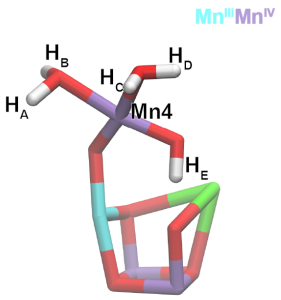

Figure S11: Labels for protons on W1, W2 and O6, which were chosen for hyperfine coupling constant calculations.

Table S13: Scaled isotropic hyperfine coupling constants (A_{iso}) in MHz of protons in OEC ligands.

H name	$A_{\mathrm{iso},\alpha\alpha\beta\alpha\alpha}$ (MHz)	$A_{\mathrm{iso},\alpha\alpha\beta\alpha\beta}$ (MHz)	$A_{\mathrm{iso,average}}$ (MHz)
H_A	0.7	0.7	0.7
H_B	0.9	0.9	0.9
H_C	0.8	0.8	0.8
H_D	0.9	0.9	0.9
H_E	4.6	4.6	4.6

The ORCA input for EPR g tensor and proton hyperfine coupling constants calculation, the *orca_ eca* utility input file, and the Python code for SVD calculation of exchange coupling constants (J) are provided in the QMMM folder of our github page.

References

(1) Umena, Y.; Kawakami, K.; Shen, J. R.; Kamiya, N. Crystal structure of oxygen-evolving photosystem II at a resolution of 1.9 Å. *Nature* **2011**, *473*, 55–60.

(2) Yang, K. R.; Lakshmi, K. V.; Brudvig, G. W.; Batista, V. S. Is deprotonation of the oxygen-evolving complex of photosystem II during the $S_1 \rightarrow S_2$ transitions suppressed by proton quantum delocalization? *J. Am. Chem. Soc.* **2021**, *143*, 8324–8332.

(3) Isobe, H.; Shoji, M.; Shen, J.-R.; Yamaguchi, K. Strong coupling between the hydrogen

bonding environment and redox chemistry during the S_2 to S_3 transition in the oxygen-evolving complex of photosystem II. *J. Phys. Chem. B* **2015**, *119*, 13922–13933.

(4) Vreven, T.; Morokuma, K. The ONIOM (our own N-layered integrated molecular orbital + molecular mechanics) method for the first singlet excited (S_1) state photoisomerization path of a retinal protonated Schiff base. *J. Chem. Phys.* **2000**, *113*, 2969–2975.

(5) Frisch, M. J. et al. Gaussian 16 Revision C.01. 2016; Gaussian Inc. Wallingford CT.

(6) Becke, A. D. Density-functional thermochemistry. III. The role of exact exchange. *J. Chem. Phys.* **1993**, *98*, 5648–5652.

(7) Lee, C.; Yang, W.; Parr, R. G. Development of the Colle-Salvetti correlation-energy formula into a functional of the electron density. *Phys. Rev. B* **1988**, *37*, 785–789.

(8) Vosko, S. H.; Wilk, L.; Nusair, M. Accurate spin-dependent electron liquid correlation energies for local spin density calculations: a critical analysis. *Can. J. Phys.* **1980**, *58*, 1200–1211.

(9) Stephens, P. J.; Devlin, F. J.; Chabalowski, C. F.; Frisch, M. J. Ab Initio Calculation of Vibrational Absorption and Circular Dichroism Spectra Using Density Functional Force Fields. *J. Phys. Chem.* **1994**, *98*, 11623–11627.

(10) Hay, P. J.; Wadt, W. R. Ab initio effective core potentials for molecular calculations. Potentials for K to Au including the outermost core orbitals. *J. Chem. Phys.* **1985**, *82*, 299–310.

(11) da Silva Filho, D. A.; Coropceanu, V.; Fichou, D.; Gruhn, N. E.; Bill, T. G.; Gierschner, J.; Cornil, J.; Brédas, J.-L. Hole-vibronic coupling in oligothiophenes: impact of backbone torsional flexibility on relaxation energies. *Philos. Trans. R. Soc. A* **2007**, *365*, 1435–1452.

(12) Hariharan, P. C.; Pople, J. A. The influence of polarization functions on molecular orbital hydrogenation energies. *Theoret. Chim. Acta* **1973**, *28*, 213–222.

(13) Sproviero, E. M.; Gascon, J. A.; McEvoy, J. P.; Brudvig, G. W.; Batista, V. S. Characterization of synthetic oxomanganese complexes and the inorganic core of the O_2-evolving complex in photosystem II: evaluation of the DFT/B3LYP level of theory. *J. Inorg. Biochem.* **2006**, *100*, 786–800.

(14) Wang, T.; Brudvig, G.; Batista, V. S. Characterization of proton coupled electron transfer in a biomimetic oxomanganese complex: Evaluation of the DFT B3LYP level of theory. *J. Chem. Theory Comput.* **2010**, *6*, 755–760.

(15) Luo, S.; Rivalta, I.; Batista, V.; Truhlar, D. G. Noncollinear Spins Provide a Self-Consistent Treatment of the Low-Spin State of a Biomimetic Oxomanganese Synthetic Trimer Inspired by the Oxygen Evolving Complex of Photosystem II. *J. Phys. Chem. Lett.* **2011**, *2*, 2629–2633.

(16) Cornell, W. D.; Cieplak, P.; Bayly, C. I.; Gould, I. R.; Merz, K. M.; Ferguson, D. M.; Spellmeyer, D. C.; Fox, T.; Caldwell, J. W.; Kollman, P. A. A Second Generation Force Field for the Simulation of Proteins, Nucleic Acids, and Organic Molecules. *J. Am. Chem. Soc.* **1995**, *117*, 5179–5197.

(17) Humphrey, W.; Dalke, A.; Schulten, K. VMD – Visual Molecular Dynamics. *J. Mol. Graphics* **1996**, *14*, 33–38.

(18) Guskov, A.; Kern, J.; Gabdulkhakov, A.; Broser, M.; Zouni, A.; Saenger, W. Cyanobacterial photosystem II at 2.9-Å resolution and the role of quinones, lipids, channels and chloride. *Nat. Struct. Mol. Biol.* **2009**, *16*, 334–342.

(19) Suga, M.; Akita, F.; Hirata, K.; Ueno, G.; Murakami, H.; Nakajima, Y.; Shimizu, T.; Yamashita, K.; Yamamoto, M.; Ago, H.; Shen, J. R. Native structure of photosystem II at 1.95 Å resolution viewed by femtosecond X-ray pulses. *Nature* **2015**, *517*, 99–103.

(20) Kaur, D.; Zhang, Y.; Reiss, K. M.; Mandal, M.; Brudvig, G. W.; Batista, V. S.; Gunner, M. Proton exit pathways surrounding the oxygen evolving complex of photosystem II. *Biochim. Biophys. Acta – Bioener.* **2021**, *1862*, 148446.

(21) Bas, D. C.; Rogers, D. M.; Jensen, J. H. Very fast prediction and rationalization of pKa values for protein-ligand complexes. *Proteins* **2008**, *73*, 765–783.

(22) Huang, J.; Rauscher, S.; Nawrocki, G.; Ran, T.; Feig, M.; de Groot, B. L.; ller, H.; MacKerell, A. D. CHARMM36m: an improved force field for folded and intrinsically disordered proteins. *Nat. Methods* **2017**, *14*, 71–73.

(23) Guerra, F.; Adam, S.; Bondar, A.-N. Revised force-field parameters for chlorophyll-a, pheophytin-a and plastoquinone-9. *J. Mol. Graph. Model.* **2015**, *58*, 30–39.

(24) Vanommeslaeghe, K.; Hatcher, E.; Acharya, C.; Kundu, S.; Zhong, S.; Shim, J.; Darian, E.; Guvench, O.; Lopes, P.; Vorobyov, I.; Mackerell, A. D. CHARMM general force field: A force field for drug-like molecules compatible with the CHARMM all-atom additive biological force fields. *J. Comput. Chem.* **2010**, *31*, 671–690.

(25) Adam, S.; Knapp-Mohammady, M.; Yi, J.; Bondar, A.-N. Revised CHARMM force field parameters for iron-containing cofactors of photosystem II. *J. Comput. Chem.* **2018**, *39*, 7–20.

(26) Lee, J. et al. CHARMM-GUI Membrane Builder for Complex Biological Membrane Simulations with Glycolipids and Lipoglycans. *J. Chem. Theory Comput.* **2019**, *15*, 775–786.

(27) Li, Y.; Liu, J.; Gumbart, J. C. In *Structure and Function of Membrane Proteins*; Schmidt-Krey, I., Gumbart, J. C., Eds.; Springer US: New York, NY, 2021; pp 237–251.

(28) Staehelin, L. A.; van der Staay, G. W. M. *Oxygenic Photosynthesis: The Light Reactions*; Springer Netherlands: Dordrecht, 1996; pp 11–30.

(29) Mizusawa, N.; Wada, H. The role of lipids in photosystem II. *Biochim. Biophys. Acta – Bioener.* **2012**, *1817*, 194–208.

(30) Sakurai, I.; Shen, J.-R.; Leng, J.; Ohashi, S.; Kobayashi, M.; Wada, H. Lipids in oxygen-evolving photosystem II complexes of cyanobacteria and higher plants. *J. Biochem.* **2006**, *140*, 201–209.

(31) Klauda, J. B.; Venable, R. M.; Freites, J. A.; O'Connor, J. W.; Tobias, D. J.; Mondragon-Ramirez, C.; Vorobyov, I.; MacKerell, A. D.; Pastor, R. W. Update of the CHARMM all-atom additive force field for lipids: validation on six lipid types. *J. Phys. Chem. B* **2010**, *114*, 7830–7843.

(32) Cárdenas, G.; Marquetand, P.; Mai, S.; González, L. A Force Field for a Manganese-Vanadium Water Oxidation Catalyst: Redox Potentials in Solution as Showcase. *Catalysts* **2021**, *11*.

(33) Won, Y. Force Field for Monovalent, Divalent, and Trivalent Cations Developed under the Solvent Boundary Potential. *J. Phys. Chem. A* **2012**, *116*, 11763–11767.

(34) Jorgensen, W. L.; Chandrasekhar, J.; Madura, J. D.; Impey, R. W.; Klein, M. L. Comparison of simple potential functions for simulating liquid water. *J. Chem. Phys.* **1983**, *79*, 926–935.

(35) Venable, R. M.; Luo, Y.; Gawrisch, K.; Roux, B.; Pastor, R. W. Simulations of Anionic Lipid Membranes: Development of Interaction-Specific Ion Parameters and Validation Using NMR Data. *J. Phys. Chem. B* **2013**, *117*, 10183–10192.

(36) Kaur, D.; Reiss, K.; Wang, J.; Batista, V. S.; Brudvig, G. W.; Gunner, M. R. Occupancy Analysis of Water Molecules inside Channels within 25 Å Radius of the Oxygen-

Evolving Center of Photosystem II in Molecular Dynamics Simulations. *J. Phys. Chem. B* **2024**, *128*, 2236–2248.

(37) Ishikita, H.; Saito, K. Proton transfer reactions and hydrogen-bond networks in protein environments. *J. R. Soc. Interface* **2014**, *11*, 20130518.

(38) Flesher, D. A.; Liu, J.; Wiwczar, J. M.; Reiss, K.; Yang, K. R.; Wang, J.; Askerka, M.; Gisriel, C. J.; Batista, V. S.; Brudvig, G. W. Glycerol binding at the narrow channel of photosystem II stabilizes the low-spin S_2 state of the oxygen-evolving complex. *Photosyn. Res.* **2022**, *152*, 167–175.

(39) Hussein, R. et al. Structural dynamics in the water and proton channels of photosystem II during the S_2 to S_3 transition. *Nat. Commun.* **2021**, *12*, 6531.

(40) Pantazis, D. A.; Orio, M.; Petrenko, T.; Zein, S.; Bill, E.; Lubitz, W.; Messinger, J.; Neese, F. A New Quantum Chemical Approach to the Magnetic Properties of Oligonuclear Transition-Metal Complexes: Application to a Model for the Tetranuclear Manganese Cluster of Photosystem II. *Chem. Eur. J.* **2009**, *15*, 5108–5123.

(41) Neese, F. The ORCA program system. *Wiley Interdiscip. Rev. Comput. Mol. Sci.* **2012**, *2*, 73–78.

(42) Neese, F.; Wennmohs, F.; Becker, U.; Riplinger, C. The ORCA quantum chemistry program package. *J. Chem. Phys.* **2020**, *152*, 224108.

(43) Neese, F. Software update: The ORCA program system—Version 5.0. *Wiley Interdiscip. Rev. Comput. Mol. Sci.* **2022**, *12*, e1606.

(44) van Lenthe, E.; Baerends, E. J.; Snijders, J. G. Relativistic total energy using regular approximations. *J. Chem. Phys.* **1994**, *101*, 9783–9792.

(45) van Wüllen, C. Molecular density functional calculations in the regular relativistic approximation: Method, application to coinage metal diatomics, hydrides, fluorides

and chlorides, and comparison with first-order relativistic calculations. *J. Chem. Phys.* **1998**, *109*, 392–399.

(46) Pantazis, D. A.; Ames, W.; Cox, N.; Lubitz, W.; Neese, F. Two interconvertible structures that explain the spectroscopic properties of the oxygen-evolving complex of photosystem II in the S_2 State. *Angew. Chem. Int. Ed. Engl.* **2012**, *51*, 9935–9940.

(47) Cox, N.; Retegan, M.; Neese, F.; Pantazis, D. A.; Boussac, A.; Lubitz, W. Electronic structure of the oxygen-evolving complex in photosystem II prior to O-O bond formation. *Science* **2014**, *345*, 804–808.